Analytical treatment of near-field electromagnetic heat transfer at the nanoscale

Hideo Iizuka[1] and Shanhui Fan[2]

[1]*Toyota Central Research and Development Labs, Nagakute, Aichi 480 1192, Japan*

[2]*Department of Electrical Engineering, Ginzton Laboratory, Stanford University, Stanford, California 94305, USA*

(Received 21 May 2015; revised manuscript received 26 September 2015; published 15 October 2015)

Near-field thermal transfer between material bodies is generally obtained by numerical calculation methods. We present simple close-form analytic results for heat transfer between planar structures, derived by explicitly relating the heat transfer to the dispersion relations of the coupled systems. In the conventional case of heat transfer between SiC slabs, the closed-form analytic results agree excellently with numerical simulations. In the case where two graphene sheets are separated by a distance d, our theory shows that the heat transfer scales as $1/d$, rather than $1/d^2$ as in the conventional cases, due to the unique dispersion relation of two-dimensional plasmons.

DOI: 10.1103/PhysRevB.92.144307 PACS number(s): 44.40.+a, 44.05.+e, 05.40.−a

I. INTRODUCTION

There has been a large body of theoretical works on near-field electromagnetic heat transfer in the nanoscale [1–23], both due to fundamental interests since the transfer can significantly exceed the far field limit [24–31] and also due to the potential for practical applications such as energy conversion [32,33], cooling [34], and nanoscale imaging [35–37]. However, most of these papers have used numerical simulations, while the analytic understanding has been lacking. This is true even for the simplest case between two parallel surfaces separated by a spacing d in vacuum. By considering the maximum number of wave channels available in vacuum and utilizing conceptual tools such as quantum information theory [38] or mesoscopic quantum transport [39], a number of authors have derived an upper limit for heat conductance [38–43], which diverges as $1/d^2$, as d approaches nanoscale, in consistency with the numerical simulations [2,33]. However, these derived upper limits are orders of magnitude larger than the actual heat conductance. To our knowledge, there has not been any analytic derivation showing the $1/d^2$ dependency of heat transfer in realistic materials. In addition, since most of these analytic treatments have focused on the property of vacuum [38,39], the role of the material properties is not transparent in these treatments, in spite of the numerical observations of the prominent role that surface waves play.

In this paper, we present a fully analytic theory that provides simple close-form formulas for the heat transfer between two surfaces separated by vacuum with a distance d. The key advancement here is to establish a quantitative link between the heat transfer and the dispersion relations of the coupled surface waves. Our general formula of the quantitative link [Eq. (19) in this paper] is applicable for both the three-dimensional (3D) and the two-dimensional (2D) systems supporting plasmon or phonon polaritons. In the case of thermal transfer between two SiC regions, the resulting formula [Eq. (24)] excellently agrees with numerical results. With the same approach, we have also considered the near-field transfer between two graphene layers and shown analytically that the 2D plasmon in graphene gives rise to a $1/d$ behavior in the thermal transfer [Eq. (33)], as opposed to the $1/d^2$ behavior in typical systems supporting 3D plasmon or phonon polaritons. Thus, we predict that 2D plasmon will have a distinctively different signature in near-field heat transfer as compared to 3D surface plasmon systems.

This paper is organized as follows. In Sec. II, we present the configurations, a brief review of the fluctuational electrodynamics, and an upper limit of heat transfer. We present our formalism in Sec. III and compare analytical and numerical results in Sec. IV. This paper is then concluded in Sec. V.

II. CONFIGURATIONS AND NUMERICAL CALCULATION METHOD

A. Configurations

We start by considering the thermal transfer between parallel surfaces of identical bodies with temperatures T and $T+\delta T$ through a vacuum gap. Here, we select the SiC plates and graphene layers as typical 3D and 2D systems supporting phonon or plasmon polaritons as shown in Figs. 1(a) and 1(b).

In the SiC case, the permittivity of SiC is expressed as

$$\varepsilon(\omega)=\varepsilon_\infty\left[1+\frac{{\omega_{\mathrm{LO}}}^2-{\omega_{\mathrm{TO}}}^2}{{\omega_{\mathrm{TO}}}^2-\omega^2-i\gamma_m\omega}\right], \tag{1}$$

where $\omega_{\mathrm{LO}}=969\,\mathrm{cm}^{-1}$, $\omega_{\mathrm{TO}}=793\,\mathrm{cm}^{-1}$, $\gamma_m=4.76\,\mathrm{cm}^{-1}$, and $\varepsilon_\infty=6.7$ [2].

In the graphene case, the optical conductivity of graphene, including both the Drude and interband contributions, is expressed as

$$\sigma=i\frac{2e^2k_BT}{\pi\hbar^2(\omega+i\gamma_m)}\ln\left\{2\cosh\left[\frac{\mu}{2k_BT}\right]\right\}+\frac{e^2}{4\hbar}\left[G\left(\frac{\hbar\omega}{2}\right)+i\frac{4\hbar\omega}{\pi}\int_0^\infty\frac{G(\xi)-G\left(\frac{\hbar\omega}{2}\right)}{(\hbar\omega)^2-4\xi^2}d\xi\right], \tag{2}$$

where $G(\xi)=\frac{\sinh\frac{\xi}{k_BT}}{\cosh\frac{\mu}{k_BT}+\cosh\frac{\xi}{k_BT}}$ [44]. We assume a damping rate of $\gamma_m=10^{13}$ rad/s, and a chemical potential of $\mu=0.3$ eV for graphene [8–10].

B. Fluctuational electrodynamics

We consider the limit of a small gap size d, such that the evanescent waves dominantly contribute to the heat transfer. Using the fluctuational electrodynamics formalism, the heat

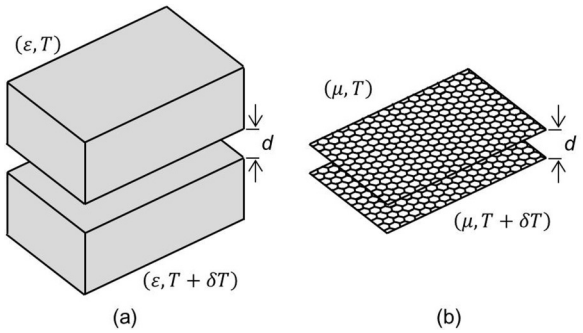

FIG. 1. Configurations of parallel surfaces of identical material bodies with temperatures T and $T+\delta T$. (a) Silicon carbide plates. (b) Graphene layers.

transfer coefficient is derived as [33]

$$h=\frac{\partial}{\partial T}\int_{k_0}^{+\infty}\frac{\beta d\beta}{2\pi}\int_0^{+\infty}\frac{d\omega}{2\pi}\frac{4\{\mathrm{Im}[r(\omega,\beta)]\}^2e^{-2\kappa_0 d}}{|1-r(\omega,\beta)^2e^{-2\kappa_0 d}|^2}\Theta(\omega,T\ ), \tag{3}$$

where $r(\omega,\beta)$ is the Fresnel reflection coefficient of the evanescent waves at the body-vacuum interface, $\Theta(\omega,T)=\frac{\hbar\omega}{e^{\hbar\omega/(k_BT)}-1}$ is the mean thermal energy of a single optical mode, $\hbar$ and k_B are the reduced Planck constant and the Boltzmann constant, respectively, and β is the wavenumber component parallel to the interface. The normal wavenumber in vacuum has the form of $\kappa_0=\sqrt{\beta^2-k_0^2}$ ($k_0<\beta$), where k_0 is the free space wavenumber. To arrive at Eq. (3), we have assumed that only the p polarization contributes significantly to the heat transfer since the near-field heat transfer for the systems we consider in this paper is dominated by surface-polariton excitations, which are p-polarized waves. Also, this formula is applicable in the classical regime and does not apply when the separation between the bodies is at a single nanometer scale, and hence quantum mechanical effects need to be taken into account [45–47].

The normalized exchange function $Z(\omega,\beta)\equiv\frac{4\{\mathrm{Im}[r(\omega,\beta)]\}^2e^{-2\kappa_0 d}}{|1-r(\omega,\beta)^2e^{-2\kappa_0 d}|^2}$ in the integrand characterizes the contribution at a frequency ω and wavenumber β. One can rigorously prove that $0\leqslant Z\leqslant 1$. The normalized exchange function Z is multiplied by $\Theta(\omega,T)$ for the absolute amount of heat transfer.

For the SiC case, the Fresnel reflection coefficient of the evanescent p polarization at the plate-vacuum interface is given by [33]

$$r(\omega,\beta)=\frac{\varepsilon(\omega)\kappa_0-\kappa}{\varepsilon(\omega)\kappa_0+\kappa}, \tag{4}$$

where $\kappa=\sqrt{\beta^2-\varepsilon k_0^2}$. For the graphene case, the reflection coefficient of the evanescent p polarization at the graphene-vacuum interface is given by [8]

$$r(\omega,\beta)=\frac{1}{1-i\frac{2\varepsilon_0\omega}{\sigma\kappa_0}}. \tag{5}$$

The heat transfer coefficients for the SiC and the graphene cases are numerically obtained by substituting Eqs. (1), (4) and Eqs. (2), (5), respectively, into Eq. (3).

In Eq. (3), the heat transfer is treated as a summation of independent channels indexed by the lateral wavenumber β, and therefore, we define as

$$h=\int_{k_0}^{+\infty}\frac{\beta d\beta}{2\pi}h_s(\beta), \tag{6}$$

where channel heat transfer coefficient

$$h_s(\beta)=\frac{\partial}{\partial T}\int_0^{+\infty}\frac{d\omega}{2\pi}\frac{4\{\mathrm{Im}[r(\omega,\beta)]\}^2e^{-2\kappa_0 d}}{|1-r(\omega,\beta)^2e^{-2\kappa_0 d}|^2}\Theta(\omega,T\ ). \tag{7}$$

The channel heat transfer coefficients for the SiC and the graphene cases are numerically obtained by substituting Eqs. (1), (4) and Eqs. (2), (5), respectively, into Eq. (7).

C. Upper limit of heat transfer

Equation (3) has been used as the starting point for analytic treatment of near-field heat transfer in Refs. [38,40–42]. To analytically evaluate Eq. (3), Refs. [38,40–42] made two assumptions: (1) only channels with $\beta\leqslant\beta_c=\frac{\pi}{d}$ contribute; (2) for each contributing channel, one assumes $Z(\omega,\beta)=1$ for all frequencies. With these two assumptions, the integral in Eq. (3) can be evaluated as

$$h_u=\frac{\pi^2k_B^2T}{24\hbar d^2}, \tag{8}$$

which defines an upper limit h_u of heat transfer between two planar bodies separated by a distance d. This result has been quite influential in the study of near-field heat transfer.

To motivate our own theoretical work here, however, it is instructive to compare Eq. (8) to numerical simulation of a realistic material case: heat transfer between identical SiC plates. The heat transfer coefficient, obtained numerically using the method outlined in the section above, is plotted as a function of the gap size d in Fig. 2(a) as the pink dots. We see that the heat transfer coefficient has the $1/d^2$ dependency, but its value is below Eq. (8) [green dashed curve in Fig. 2(a)] by several orders of magnitude. Therefore, while Eq. (8) indeed is an appropriate upper bound, one cannot use Eq. (8) to account for heat transfer in realistic materials.

The discrepancy between Eq. (8) and the numerical simulation can be understood by plotting the normalized exchange function $Z(\omega,\beta)$ as shown in Fig. 2(b). Unlike the assumption made for Eq. (8), where $Z=1$ for all ω and β with $\beta\leqslant\beta_c$, (i.e. $Z=1$ for the entire ω-β phase space to the left of the green dashed line in Fig. 2(b), $Z(\omega,\beta)$ for realistic materials reaches near unity [white-color regions in Fig. 2(b)] only in the vicinity of the dispersion relation of the plate-plate structure, which is described by [14,33]

$$\left(\frac{\varepsilon(\omega)}{\kappa}+\frac{1}{\kappa_0}\right)^2e^{\kappa_0 d}-\left(\frac{\varepsilon(\omega)}{\kappa}-\frac{1}{\kappa_0}\right)^2e^{-\kappa_0 d}=0. \tag{9}$$

Equation (9) is solved with a real β and complex ω [48], and the real part of ω is plotted as the pink solid line in Fig. 2(b). Away from the dispersion relation $Z(\omega,\beta)$ is essentially zero [black-color regions in Fig. 2(b)]. Therefore, it is not surprising that Eq. (8) vastly overestimates the strength of heat exchange in realistic materials.

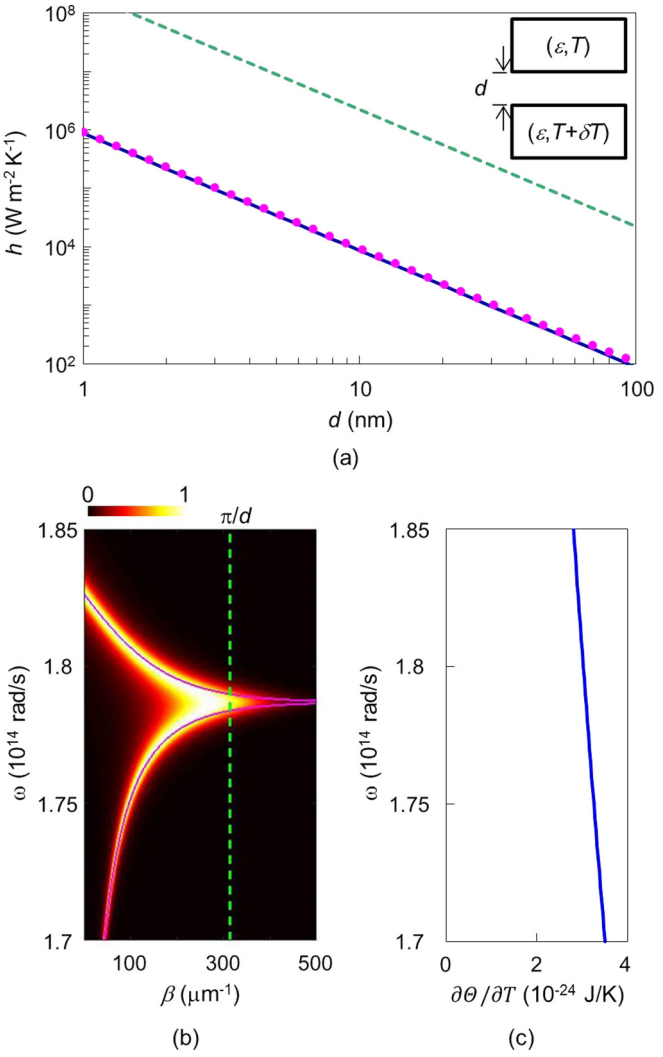

FIG. 2. (Color online) (a) Distance dependency of the heat transfer coefficient between identical silicon carbide plates at $T = 300\,\mathrm{K}$ [blue solid line: analytic theory, Eq. (24); pink dots: fluctuational electrodynamics, Eqs. (1), (3), and (4)]. (b) Normalized exchange function $Z(\omega,\beta) \equiv \frac{4[\mathrm{Im}[r(\omega,\beta)]]^2 e^{-2\kappa_0 d}}{|1-r(\omega,\beta)^2 e^{-2\kappa_0 d}|^2}$ at $d = 10\,\mathrm{nm}$. $Z(\omega,\beta)$ varies from 0 to 1 [as represented by regions with colors varying from black to white in (b)] in the ω-β phase space. The dispersion curve (pink solid line) is obtained from Eq. (9). For each figure, the green dashed line represents an upper limit based on Eq. (8) in (a) and the cutoff wavenumber $\beta_c = \frac{\pi}{d}$ in (b). (c) Mean thermal energy of a single optical mode as a function of frequency in the frequency range near the surface phonon-polariton frequency of SiC.

III. FORMALISM

In order to obtain a close-form analytic evaluation of Eq. (3), one needs to establish a quantitative link between the normalized exchange function Z and the dispersion relation of the surface waves. Below, we illustrate our approach for establishing such a link, first for the SiC case and then for the graphene case.

A. SiC case

We start with the discussion of the dispersion relation. We consider the lossless case first. Assuming that a single interface supports a single surface wave mode with a dispersion relation of ω_s, we then have

$$r(\omega_s,\beta) = \infty. \tag{10}$$

In other words, the surface wave mode of a single interface is a pole of the reflection coefficient for the evanescent wave at the same interface [49]. With two interfaces for the structure, as shown in Fig. 1, the surface wave modes at the two interfaces then couple, resulting in two modes as described by dispersion relations ω_H and ω_L, respectively. In terms of the reflection coefficients then, we need to have

$$r(\omega_H,\beta) = -\frac{1}{e^{-\beta d}}, \tag{11}$$

$$r(\omega_L,\beta) = \frac{1}{e^{-\beta d}}, \tag{12}$$

such that the evanescent wave going through a round trip between the two surfaces maintains its amplitude.

A single SiC-vacuum interface supports a surface phonon resonance at $\varepsilon(\omega_s) = -1$ with $\omega_s = \sqrt{\frac{\varepsilon_\infty \omega_{\mathrm{LO}}^2 + \omega_{\mathrm{TO}}^2}{\varepsilon_\infty + 1}}$ [14] in the lossless case. In addition, from the dispersion relation of the plate-plate structure of Eq. (9), and considering the regime of $\beta \gg k_0$, we obtain the dispersion relation of the common and the differential mode for the plate-plate structure as $\omega_H(\beta) = \omega_s\sqrt{\frac{1+A_1 e^{-\beta d}}{1+A_2 e^{-\beta d}}}$ and $\omega_L(\beta) = \omega_s\sqrt{\frac{1-A_1 e^{-\beta d}}{1-A_2 e^{-\beta d}}}$, respectively, where $A_1 = \frac{\varepsilon_\infty \omega_{\mathrm{LO}}^2 - \omega_{\mathrm{TO}}^2}{\varepsilon_\infty \omega_{\mathrm{LO}}^2 + \omega_{\mathrm{TO}}^2}$ and $A_2 = \frac{\varepsilon_\infty - 1}{\varepsilon_\infty + 1}$. One can check that ω_s, $\omega_H(\beta)$, and $\omega_L(\beta)$ satisfy Eqs. (10)–(12).

Next, we consider the lossy case. In the $\beta \gg k_0$ regime, the reflection coefficient of Eq. (4) is approximately given by

$$r(\omega,\beta) \approx \frac{\varepsilon(\omega) - 1}{\varepsilon(\omega) + 1}. \tag{13}$$

Substituting the permittivity of SiC of Eq. (1) into Eq. (13), we have

$$r(\omega,\beta) = \frac{A_2\omega^2 - A_1\omega_s^2 + iA_2\omega\gamma_m}{\omega^2 - \omega_s^2 + i\omega\gamma_m}, \tag{14}$$

where A_1 and A_2 are written with ω_s, ω_H, and ω_L

$$A_1 = \frac{\omega_s^2(\omega_H^2 + \omega_L^2) - \omega_H^2\omega_L^2}{\omega_s^2(\omega_H^2 - \omega_L^2)e^{-\beta d}}, \tag{15}$$

$$A_2 = \frac{2\omega_s^2 - (\omega_H^2 + \omega_L^2)}{(\omega_H^2 - \omega_L^2)e^{-\beta d}}. \tag{16}$$

Substituting Eqs. (15) and (16) into Eq. (14), we have the reflection coefficient

$$r(\omega,\beta) = -\frac{(\omega_s^2 - \omega_L^2)(\omega_H^2 - \omega^2) + (\omega_H^2 - \omega_s^2)(\omega^2 - \omega_L^2) - i\gamma_m\omega[(\omega_s^2 - \omega_L^2) - (\omega_H^2 - \omega_s^2)]}{(\omega_H^2 - \omega_L^2)(\omega + \omega_s)[(\omega - \omega_s) + \frac{i\gamma_m\omega}{\omega+\omega_s}]e^{-\beta d}}. \tag{17}$$

Thus, we have expressed the reflection coefficient in terms of the dispersion relation of surface polariton modes at the interfaces. We expect that the real part of the pole of $r(\omega,\beta)$ remains very close to ω_s, and the imaginary part of the pole is equal to $\frac{\gamma_m}{2}$ [50]. Equation (17) satisfies these expectations. In deriving Eq. (17), we only assumed $\kappa_0 \approx \kappa \approx \beta$, which is applicable in the small d limit where the dominant channel of heat transfer satisfies $\beta \gg k_0$.

We next perform the frequency integration of Eq. (3) analytically. We substitute Eq. (17) into Eq. (3) and in the limit of $\omega_H^2 \gg (\frac{\gamma_m}{2})^2$ and $\omega_L^2 \gg (\frac{\gamma_m}{2})^2$, we obtain

$$h \approx \frac{\partial}{\partial T}\int_{k_0}^{+\infty}\frac{\beta d\beta}{2\pi}\int_0^{+\infty}\frac{d\omega}{2\pi}\frac{\left(\omega_H^2-\omega_L^2\right)^2\gamma_m^2\omega^2\Theta(\omega,T)}{\left[\omega-\left(\omega_L+i\frac{\gamma_m}{2}\right)\right]\left[\omega-\left(\omega_L-i\frac{\gamma_m}{2}\right)\right]\left[\omega-\left(-\omega_L+i\frac{\gamma_m}{2}\right)\right]\left[\omega-\left(-\omega_L-i\frac{\gamma_m}{2}\right)\right]} \times\frac{1}{\left[\omega-\left(\omega_H+i\frac{\gamma_m}{2}\right)\right]\left[\omega-\left(\omega_H-i\frac{\gamma_m}{2}\right)\right]\left[\omega-\left(-\omega_H+i\frac{\gamma_m}{2}\right)\right]\left[\omega-\left(-\omega_H-i\frac{\gamma_m}{2}\right)\right]}. \quad (18)$$

Then we perform a contour integration in the complex ω plane. Four poles, $\omega=\pm\omega_L+\frac{i\gamma_m}{2}$ and $\omega=\pm\omega_H+\frac{i\gamma_m}{2}$ in the upper half of the complex plane, which correspond to the surface polariton resonances of the system, have dominant contribution, whereas the contributions from a set of poles on the imaginary axis arising from the term $\Theta(\omega,T)$ are very weak. Including only the poles from the surface polariton resonance, which is justified as long as the linewidth of the resonance of the system is significantly less than k_BT (i.e. heat transfer dominantly occurs through the resonance), we have

$$h \approx \frac{\partial}{\partial T}\int_{k_0}^{+\infty}\frac{\beta d\beta}{2\pi}\frac{\gamma_m}{4} \times\frac{\left(\omega_H^2-\omega_L^2\right)^2[\Theta(\omega_H,T)+\Theta(\omega_L,T)]}{\left[(\omega_H-\omega_L)^2+\gamma_m^2\right]\left[(\omega_H+\omega_L)^2+\gamma_m^2\right]}, \quad (19)$$

where we have used $\int_0^{+\infty}\frac{d\omega}{2\pi}Z(\omega,\beta)\Theta(\omega,T)=(\frac{1}{2})\int_{-\infty}^{+\infty}\frac{d\omega}{2\pi}Z(\omega,\beta)\Theta(\omega,T)$ and $\Theta(-\omega_L+\frac{i\gamma_m}{2},T)\approx\Theta(\omega_L+\frac{i\gamma_m}{2},T)\approx\Theta(\omega_L,T)$ and $\Theta(-\omega_H+\frac{i\gamma_m}{2},T)\approx\Theta(\omega_H+\frac{i\gamma_m}{2},T)\approx\Theta(\omega_H,T)$. Equation (19) provides an explicit connection between the heat transfer coefficient and the surface wave dispersion relations of the individual and the coupled interfaces.

Equation (19) can be simplified in the limit of small d, since in this limit, the dominant contributions are from channels with $\beta \gg k_0$. For these β's, we have $\Theta(\omega_H,T)\approx\Theta(\omega_L,T)\approx\Theta(\omega_s,T)$, as seen in Fig. 2(c), and then obtain

$$h \approx \frac{\partial}{\partial T}\int_{k_0}^{+\infty}\frac{\beta d\beta}{2\pi}\frac{\gamma_m}{2} \times\frac{\left(\omega_H^2-\omega_L^2\right)^2\Theta(\omega_s,T)}{\left[(\omega_H-\omega_L)^2+\gamma_m^2\right]\left[(\omega_H+\omega_L)^2+\gamma_m^2\right]} = \frac{\partial}{\partial T}\int_{k_0}^{+\infty}\frac{\beta d\beta}{2\pi}\frac{\gamma_m}{2}\frac{\frac{(\omega_H-\omega_L)^2(\omega_H+\omega_L)^2}{\gamma_m^2[2(\omega_H^2+\omega_L^2)+\gamma_m^2]}\Theta(\omega_s,T)}{1+\frac{(\omega_H-\omega_L)^2(\omega_H+\omega_L)^2}{\gamma_m^2[2(\omega_H^2+\omega_L^2)+\gamma_m^2]}}. \quad (20)$$

In $(\omega_H+\omega_L)^2 \approx 2(\omega_H^2+\omega_L^2) \gg \gamma_m^2$, Eq. (20) is approximately written as

$$h \approx \frac{\partial}{\partial T}\int_{k_0}^{+\infty}\frac{\beta d\beta}{2\pi}\frac{\gamma_m}{2}\frac{\left(\frac{\omega_H-\omega_L}{\gamma_m}\right)^2\Theta(\omega_s,T)}{1+\left(\frac{\omega_H-\omega_L}{\gamma_m}\right)^2}. \quad (21)$$

Moreover, using the dispersion relation of ω_H, ω_L, and ω_s as described above, we have $\omega_H(\beta,d)-\omega_L(\beta,d)=\frac{2\gamma_m e^{-\beta d}}{\mathrm{Im}[\varepsilon(\omega_s)]}$, where $\mathrm{Im}[\varepsilon(\omega_s)]=\omega_s(\varepsilon_\infty+1)^2[\varepsilon_\infty(\omega_{\mathrm{LO}}^2-\omega_{\mathrm{TO}}^2)]^{-1}\gamma_m$ [14]. Therefore, Eq. (21) becomes

$$h \approx \frac{\partial}{\partial T}\int_{k_0}^{+\infty}\frac{\beta d\beta}{2\pi}\frac{\gamma_m}{2}\left(\frac{\left\{\frac{2e^{-\beta d}}{\mathrm{Im}[\varepsilon(\omega_s)]}\right\}^2}{1+\left\{\frac{2e^{-\beta d}}{\mathrm{Im}[\varepsilon(\omega_s)]}\right\}^2}\right)\Theta(\omega_s,T). \quad (22)$$

The term in the large parenthesis in Eq. (22) decreases with increasing β. We approximate this term as $1-H(\beta-\beta_c)$, where the H function is the Heaviside step function, and β_c is defined as

$$\beta_c=\left(\frac{1}{d}\right)\ln\left\{1+\frac{2}{\mathrm{Im}[\varepsilon(\omega_s)]}\right\}. \quad (23)$$

Here, we have used the approximation $\int_0^{\infty}\frac{(Be^{-x})^2}{[1+(Be^{-x})^2]}xdx \approx \int_0^{\ln(1+B)}xdx$ $(B>0)$. Note that, in the case of low loss materials, $\frac{\mathrm{Im}[\varepsilon(\omega_s)]}{2}\ll 1$, Eq. (23) has the same form of the cutoff wavenumber derived in Ref. [39] using the theory of mesoscopic transport. The heat transfer coefficient is finally derived from Eqs. (22) and (23)

$$h \approx \frac{\partial}{\partial T}\int_{k_0}^{\beta_c}\frac{\beta d\beta}{2\pi}\frac{\gamma_m}{2}\Theta(\omega_s,T) \approx \frac{\partial}{\partial T}\Theta(\omega_s,T)\frac{\gamma_m}{8\pi d^2}\left(\ln\left\{1+\frac{2}{\mathrm{Im}[\varepsilon(\omega_s)]}\right\}\right)^2. \quad (24)$$

We see in Eq. (24) that the heat transfer coefficient h has the well-known $1/d^2$ dependency [2,33].

B. Graphene case

The derivation above directly relates the behaviors of heat transfer to the dispersion property of surface phonon-polaritons. The 2D plasmon on a graphene sheet exhibits a very different dispersion relation [51,52] as compared to that of the surface phonon-polariton on a 3D medium. While previous papers have numerically considered heat transfer between graphene sheets [8–10], [the configuration is shown in Fig. 1(b)], there has not been any analytic treatment, to our knowledge. Here, we show that the same analytic approach that has been developed for SiC as shown above can be adopted to

generate insights into heat transfer between graphene sheets as well.

The dispersion characteristics of the single and double graphene layers are given by [8]

$$\frac{2}{\kappa_0}+i\frac{\sigma}{\varepsilon_0\omega}=0, \tag{25}$$

$$\left(\frac{2}{\kappa_0}+i\frac{\sigma}{\varepsilon_0\omega}\right)^2 e^{\kappa_0 d}+\left(\frac{\sigma}{\varepsilon_0\omega}\right)^2 e^{-\kappa_0 d}=0. \tag{26}$$

In the heat transfer, the Drude contribution is dominant. In the $\beta \gg k_0$ regime, using the lossless Drude model $\sigma=\frac{ie^2\mu}{\pi\hbar^2\omega}$, the plasmon of a single graphene layer then has the dispersion $\omega_s(\beta)=\sqrt{\frac{e^2\mu\beta}{2\pi\varepsilon_0\hbar^2}}$ as obtained from Eq. (25). The coupled graphene layers have a common and a differential mode with dispersion relations $\omega_H(\beta)=\omega_s(\beta)\sqrt{1+e^{-\beta d}}$ and $\omega_L(\beta)=\omega_s(\beta)\sqrt{1-e^{-\beta d}}$, respectively, as obtained from Eq. (26). One can explicitly check that the dispersions of $\omega_s(\beta)$, $\omega_H(\beta)$, and $\omega_L(\beta)$ satisfy Eqs. (10)–(12). Following the same procedure that led to Eq. (17), we have the reflection coefficient for the graphene case as follows. In the $\beta \gg k_0$ regime, the reflection coefficient of Eq. (5) is approximately given by

$$r(\omega,\beta)\approx\frac{1}{1-i\frac{2\varepsilon_0\omega}{\sigma\beta}}. \tag{27}$$

The Drude contribution is dominant in the heat transfer. With our choice of chemical potential $\mu=0.3\,\mathrm{eV}$, we have $e^{\mu/(2k_BT)}\gg e^{-\mu/(2k_BT)}$, and the optical conductivity in Eq. (2) is approximately given by

$$\sigma\approx i\frac{e^2\mu}{\pi\hbar^2(\omega+i\gamma_m)}=i\frac{2\varepsilon_0\omega_s^2}{(\omega+i\gamma_m)\beta}. \tag{28}$$

Substituting Eq. (28) into Eq. (27), the reflection coefficient is expressed as

$$r(\omega,\beta)=-\frac{\omega_s^2}{\omega^2-\omega_s^2+i\gamma_m\omega}. \tag{29}$$

In addition, ω_s is written with ω_H and ω_L

$$\omega_s^2=\frac{\omega_H^2-\omega_L^2}{2e^{-\beta d}}. \tag{30}$$

From Eqs. (29) and (30), we have the reflection coefficient of the graphene case as

$$r(\omega,\beta)=-\frac{\omega_H^2-\omega_L^2}{2(\omega+\omega_s)\left[(\omega-\omega_s)+\frac{i\gamma_m\omega}{(\omega+\omega_s)}\right]e^{-\beta d}}. \tag{31}$$

One can rigorously prove that Eq. (31) is a form of Eq. (17) since the relationship between $\omega_s(\beta)$, $\omega_H(\beta)$, and $\omega_L(\beta)$ in the graphene case is the same as that in the SiC case with the replacement of $A_1=1$ and $A_2=0$. Thus, substituting Eq. (31) into Eq. (3), we obtain exactly the same form as in Eq. (19). Equation (19) is therefore applicable for both the SiC and the graphene cases.

To further simplify Eq. (19), we note that, for graphene, we have $(\omega_{\mathrm{H}}-\omega_{\mathrm{L}})^2\gg(\gamma_m)^2$ and $(\omega_{\mathrm{H}}+\omega_{\mathrm{L}})^2\gg(\gamma_m)^2$, and moreover $\Theta(\omega_L,T)\gg\Theta(\omega_H,T)$ [as will be confirmed later when we discuss the numerical results in Fig. 8(c)]. Therefore, Eq. (19) is simplified as

$$h\approx\frac{\partial}{\partial T}\int_{k_0}^{+\infty}\frac{\beta d\beta}{2\pi}\frac{\gamma_m}{4}\Theta(\omega_L,T\,). \tag{32}$$

As the gap size d approaches the nanoscale, $\beta d\ll 1$, $\omega_L(\beta)\approx\beta\sqrt{\frac{e^2\mu d}{2\pi\varepsilon_0\hbar^2}}$. We then perform the β integration in Eq. (32) to obtain the heat transfer coefficient as

$$h=\frac{\gamma_m\varepsilon_0k_B^3T^2C_1}{4e^2\mu d}, \tag{33}$$

where $C_1=\int_0^\infty\frac{x^3e^x}{(e^x-1)^2}dx=7.212$. Equation (33) indicates that the heat transfer has the $1/d$ dependency on the gap size for the graphene case.

IV. COMPARISON OF THEORY TO NUMERICAL RESULTS

In this section, we compare the main analytical results as derived in the previous section, i.e. Eqs. (24) and (33), to numerical simulations. The theoretical results excellently agree with numerical simulations. We also provide a parametric study of the heat transfer as a function of damping rate and temperature and show that the numerical results are well accounted by our analytic theory. In addition, we provide numerical results for various spectral heat transfer coefficients, which confirm various approximations made in the analytic derivations above.

A. SiC case

We plot Eq. (24) for the heat transfer coefficient of the SiC plate-plate structure as a function of the distance as the blue solid line in Fig. 2(a). Equation (24) excellently agrees with the numerical result. Since the numerical evaluation of Eq. (3) gives results that have been validated experimentally [27–30], our Eq. (24) here should be directly applicable to the plate-plate experiments as well.

We plot the channel heat transfer h_s as a function of β in Fig. 3. The numerical result is obtained from Eqs. (1), (4), and (7), and the analytical result is obtained from Eqs. (6) and (22) (i.e. $h_s(\beta)=\frac{\partial}{\partial T}\frac{\gamma_m}{2}\frac{\{\frac{2e^{-\beta d}}{\mathrm{Im}[\varepsilon(\omega_s)]}\}^2}{1+\{\frac{2e^{-\beta d}}{\mathrm{Im}[\varepsilon(\omega_s)]}\}^2}\Theta(\omega_s,T\,)$). We see that h_s is almost constant up to $\beta=200\,\mu\mathrm{m}^{-1}$ and then decreases as β increases. The dominant channel wavenumber is $\beta_d=\frac{2.15}{d}$ that is obtained from $(\frac{\partial}{\partial\beta})\beta h_s=0$ in Eq. (22). The inset of Fig. 3 shows the spectral heat flux of the dominant channel at β_d. We see that strong heat transfer occurs around ω_s. There are two maxima in the heat transfer at ω_H and ω_L, respectively, where $Z(\omega,\beta)$ reaches near unity. The analytical results (blue solid lines) agree with the numerical results (pink dots) in Fig. 3. The discrepancy between the analytical and numerical results in the channel heat transfer is seen in the small β range. The discrepancy arises from the assumption of $\beta\gg k_0$ in the analytical calculations. That discrepancy of h_s has little influence on the heat transfer coefficient since the heat transfer results from a β integration of βh_s.

Substituting ω_s, ω_H, and ω_L into Eq. (17), we obtain the reflection coefficient. Using the reflection coefficient and Eq. (3), we obtain the spectrum of the heat transfer and plot it

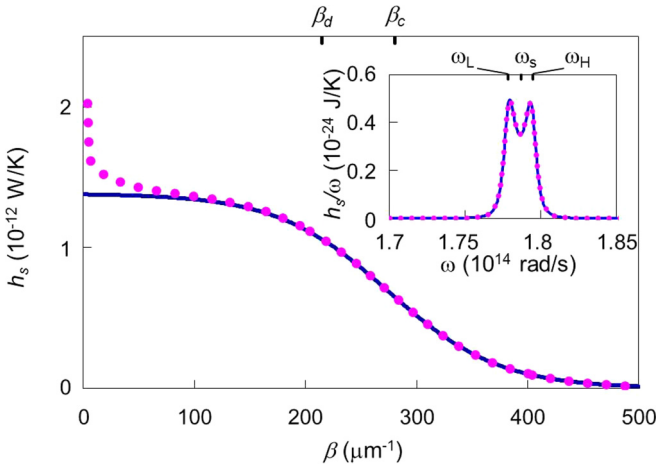

FIG. 3. (Color online) Channel heat transfer as a function of the wavenumber at $d = 10$ nm in the SiC case. The cutoff wavenumber based on Eq. (23) is $\beta_c = 281\ \mu\text{m}^{-1}$. The inset shows the spectrum of the dominant channel at $\beta_d = 215\ \mu\text{m}^{-1}$ [blue solid lines: analytic theory, Eqs. (6) and (22) for h_s and Eqs. (7) and (17) for $\frac{h_s}{\omega}$ in the inset; pink dots: fluctuational electrodynamics, Eqs. (1), (4), and (7)].

as the blue solid line in Fig. 4. We see the excellent agreement between the analytical result and the numerical result (pink dots), where the spectrum is sharply peaked. Therefore, we have verified that the resonance feature of surface waves is well characterized in our formalism.

Equation (24) shows that there exists an optimal material loss rate γ_m that maximizes the heat transfer as a result of two competing trends. We note that $\text{Im}[\varepsilon(\omega_s)] = \omega_s(\varepsilon_\infty + 1)^2[\varepsilon_\infty(\omega_{\text{LO}}^2 - \omega_{\text{TO}}^2)]^{-1}\gamma_m$. As γ_m increases, the increased material loss leads to an increase in the strength of the fluctuating current source, which however, is offset by the reduction of the cutoff wavenumber β_c. The maximum heat transfer occurs at $\text{Im}[\varepsilon(\omega_s)] \approx 0.5$, which is obtained by setting $\frac{\partial h}{\partial \gamma_m} = 0$ in Eq. (22). Such a dependency on γ_m is consistent with the numerical calculation in Ref. [23]. The

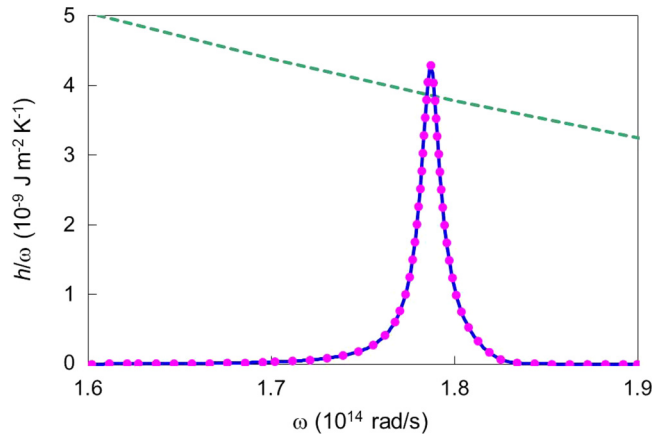

FIG. 4. (Color online) Spectrum of the heat transfer at $d = 10$ nm in the SiC case [blue solid line: analytic theory, Eqs. (3) and (17); pink dots: fluctuational electrodynamics, Eqs. (1), (3), and (4)]. The green dashed line represents an upper limit that is obtained from Eq. (3) with $Z(\omega,\beta) = 1$ for channels $\beta \leqslant \beta_c = \frac{\pi}{d}$.

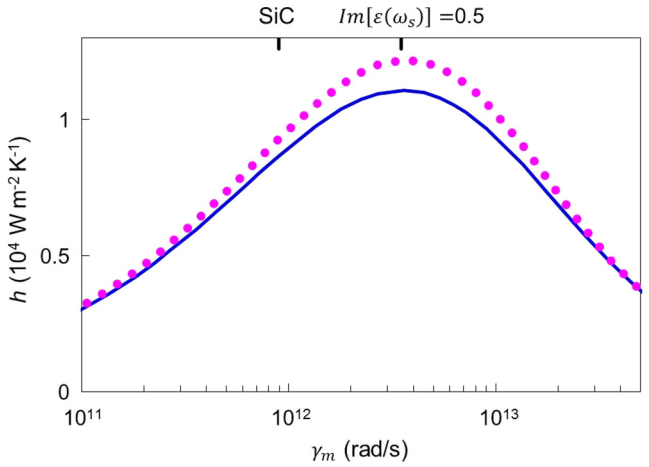

FIG. 5. (Color online) Heat transfer of Eq. (24) (blue solid line) as a function of the material damping rate γ_m. Parameters are the same as the case of Fig. 2 except for γ_m, where the distance is set at $d = 10$ nm. The fluctuational electrodynamics result [Eqs. (1), (3), and (4)] is presented by the pink dots.

heat transfer between parallel plates is calculated by Eq. (24) as the material damping rate γ_m is varied, and is plotted as the blue solid line in Fig. 5. We have used the same parameters as the case of Fig. 2 except for γ_m. We see that the heat transfer is maximized at $\text{Im}[\varepsilon(\omega_s)] \approx 0.5$ due to the two competing trends of γ_m in Eq. (24). Equation (24) agrees well with the numerical result (pink dots).

In addition, we see in Eq. (24) that the dependency on the temperature is characterized by the mean thermal energy of a single mode $\Theta(\omega_s, T)$ at the surface phonon-polariton frequency ω_s, due to the dominant heat transfer at such resonant frequency. Therefore, Eq. (24) (blue solid line) agrees well with the numerical result (pink dots) in the heat transfer behavior as a function of the temperature T (Fig. 6).

The analytic theory is not limited to SiC or materials supporting phonon polaritons. When the permittivity of a

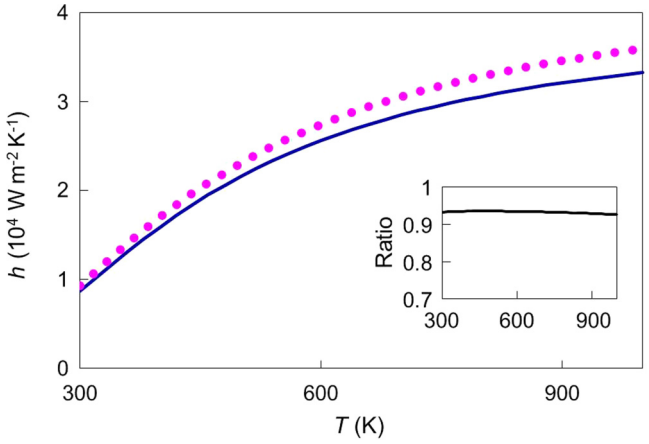

FIG. 6. (Color online) Heat transfer of Eq. (24) (blue solid line) as a function of the temperature T in the SiC case. Parameters are the same as the case of Fig. 2 except for T, where the distance is set at $d = 10$ nm. The fluctuational electrodynamics result [Eqs. (1), (3), and (4)] is presented by the pink dots. The inset shows the ratio of the analytical result to the numerical result.

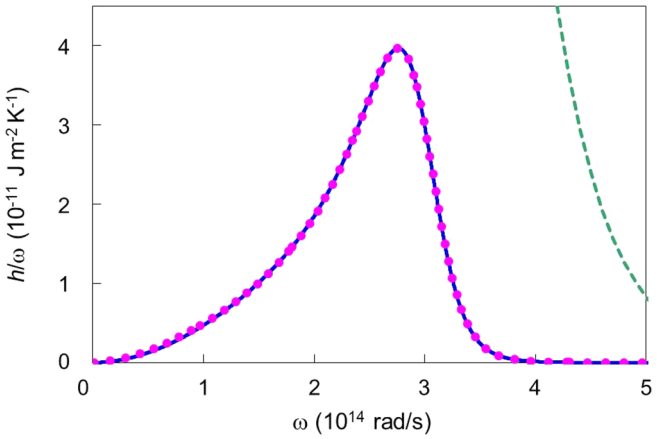

FIG. 7. (Color online) Spectrum of the heat transfer between heavily doped silicon plates at $d = 10\,\text{nm}$. The material parameters are set to be $\varepsilon_\infty = 11.7$, $\omega_p = \omega_{\text{LO}}\sqrt{\varepsilon_\infty} = 1.08 \times 10^{15}\,\text{rad/s}$, $\gamma_m = 9.34 \times 10^{13}\,\text{rad/s}$, and $\omega_{\text{TO}} = 0$ [10] in Eq. (1) [blue solid line: analytic theory, Eqs. (3), and (17); pink dots: fluctuational electrodynamics, Eqs. (1), (3), and (4)]. The green dashed line represents an upper limit that is obtained from Eq. (3) with $Z(\omega,\beta) = 1$ for channels $\beta \leqslant \beta_c = \frac{\pi}{d}$.

material is characterized by a Drude model, such as heavily doped semiconductors, the analytic theory is also applicable. One only needs to make the replacement of $\omega_p = \omega_{\text{LO}}\sqrt{\varepsilon_\infty}$ and $\omega_{\text{TO}} = 0$ in Eq. (1). Figure 7 shows the spectral heat transfer between heavily doped silicon plates. Material parameters in Eq. (1) are presented in the caption of Fig. 7 when the doping level is $10^{20}\,\text{cm}^{-3}$ [10]. We have verified the excellent agreement between Eq. (24) (blue solid line) and the numerical result (pink dots) for the heavily doped silicon case.

B. Graphene case

We plot the prediction of Eq. (33) for the heat transfer coefficient between graphene layers as a function of the distance as the blue solid line in Fig. 8(a). The analytical result agrees excellently with the numerical result (pink dots) obtained from Eqs. (2), (3), and (5), especially when the gap size d is in the deep subwavelength regime. The discrepancy between the analytic and numerical results is seen with the increase of d. The discrepancy mainly stems from the approximation of ω_L, i.e., as d increases, the approximate form of $\omega_L(\beta) \approx \beta\sqrt{\frac{e^2\mu d}{2\pi\varepsilon_0\hbar^2}}$ deviates from the exact form of $\omega_L(\beta) = \omega_s(\beta)\sqrt{1-e^{-\beta d}}$. Also, in obtaining the analytical results, the dispersion relation of the graphene plasmon [Fig. 8(b)] is obtained assuming the free electron contribution. The contribution from the interband transition is small, as we see in the numerical results shown in Fig. 8(a).

As we can see from the derivation in Sec. III B, the $1/d$ behavior of the heat transfer arises from the $\omega_L \propto \beta\sqrt{d}$ dependency in the dispersion relation of the coupled graphene sheet. Such a dependency is a direct consequence of the nature of 2D plasmons [51,52]. Examining Eq. (32), since the Planck distribution $\Theta(\omega_L,T)$ decreases as a function of ω_L, the $\omega_L \propto \beta\sqrt{d}$ dependency results in a wave vector space cutoff $\beta_c \propto 1/\sqrt{d}$, which leads to the $1/d$ dependency of the

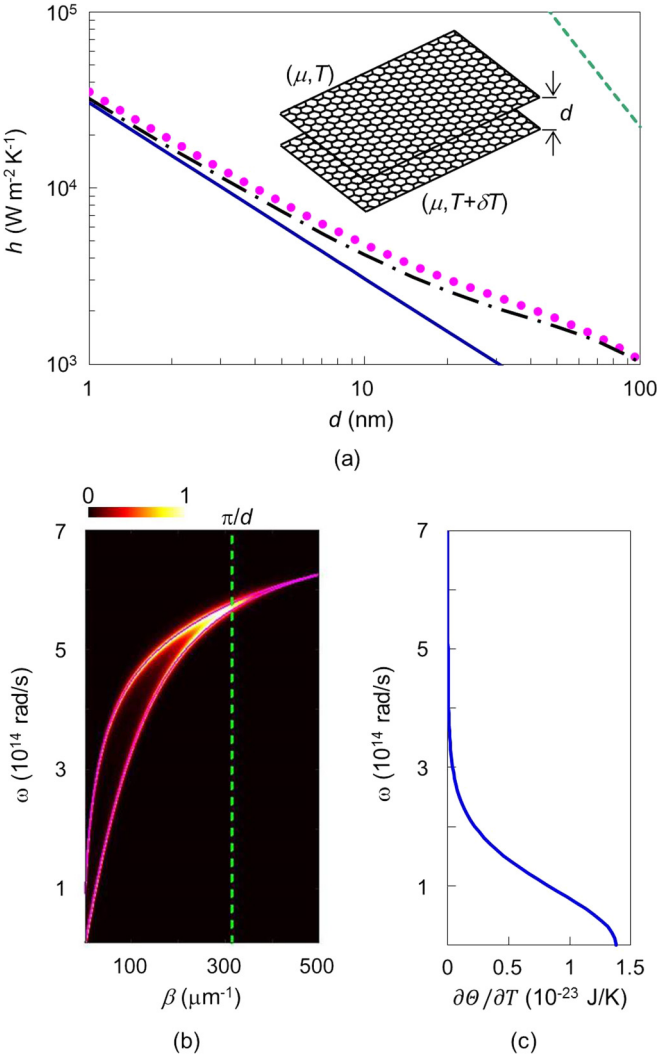

FIG. 8. (Color online) (a) Distance dependency of the heat transfer coefficient between identical graphene layers with a $\mu = 0.3\,\text{eV}$ chemical potential at a room temperature $T = 300\,\text{K}$ [blue solid line: analytical theory, Eq. (33); pink dots: fluctuational electrodynamics, Eqs. (2), (3), and (5); black dashed-dotted line: fluctuational electrodynamics considering the Drude contribution]. (b) Normalized exchange function $Z(\omega,\beta)$ at $d = 10\,\text{nm}$. The dispersion curve (pink solid line) is obtained from Eq. (26). For each figure, the green dashed line represents an upper limit based on Eq. (8) in (a) and the cutoff wavenumber $\beta_c = \frac{\pi}{d}$ in (b). (c) Mean thermal energy of a single optical mode as a function of frequency in the frequency range where a graphene layer supports 2D plasmon.

heat transfer. Such a cutoff behavior is distinctly different from the $\beta_c \propto 1/d$ behavior for the SiC case and indicates that near-field heat transfer in 2D plasmon systems is qualitatively different from its 3D counterparts.

The channel heat transfer h_s is obtained by using Eqs. (6) and (19) $\{$i.e. $h_s(\beta) = \frac{\partial}{\partial T}\frac{\gamma_m}{4}\frac{(\omega_H^2-\omega_L^2)^2[\Theta(\omega_H,T)+\Theta(\omega_L,T)]}{[(\omega_H-\omega_L)^2+\gamma_m^2][(\omega_H+\omega_L)^2+\gamma_m^2]}\}$ and plotted as a function of β in Fig. 9. We see that the analytical result (blue solid line) agrees excellently with the numerical result (pink dots). The analytical result is decomposed into the contributions of the two poles of ω_H (black dashed-dotted line) and ω_L (red dashed line). We see that the heat transfer

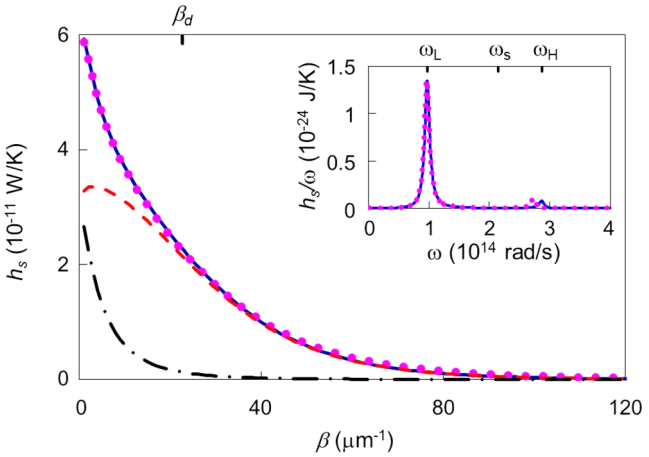

FIG. 9. (Color online) Channel heat transfer as a function of the wavenumber at $d = 10$ nm in the graphene case. The blue solid line represents the analytic result based on Eqs. (6) and (19). The analytic result is decomposed into the contributions of the two poles of ω_H (black dashed-dotted line) and ω_L (red dashed line), respectively. The pink dots represent the fluctuational electrodynamics result obtained by using Eqs. (2), (5), and (7). The inset shows the spectrum of the dominant channel at $\beta_d = 23\,\mu\text{m}^{-1}$ [blue solid line: analytic theory, Eqs. (7) and (31); pink dots: fluctuational electrodynamics].

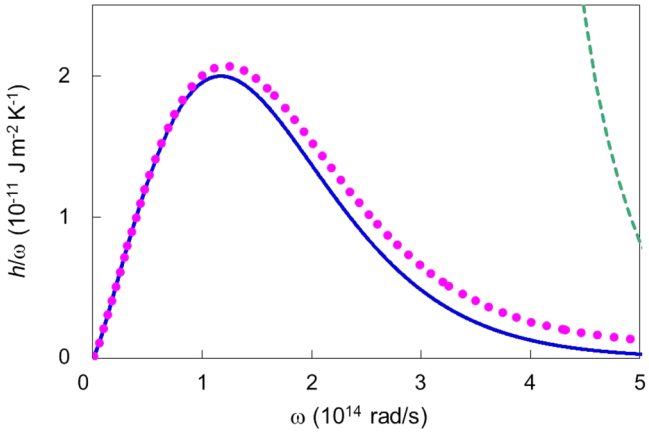

FIG. 10. (Color online) Spectrum of the heat transfer at $d = 10$ nm in the graphene case [blue solid line: analytic theory, Eqs. (3) and (31); pink dots: fluctuational electrodynamics, Eqs. (2), (3), and (5)]. The green dashed line represents an upper limit that is obtained from Eq. (3) with $Z(\omega,\beta) = 1$ for channels $\beta \leqslant \beta_c = \frac{\pi}{d}$.

dominantly occurs through ω_L, and thus, we have verified the assumption of $\Theta(\omega_L,T) \gg \Theta(\omega_H,T)$ in Eq. (32).

Substituting ω_s, ω_H, and ω_L into Eq. (31), we obtain the reflection coefficient. From the reflection coefficient and Eq. (3), we obtain the spectrum of the heat transfer and plot it as the blue solid line in Fig. 10. The heat transfer occurs in the wide spectrum. The analytical result agrees well with the numerical result (pink dots). The contribution from the interband transition is small, as we see in the comparison of the analytical and numerical results of Fig. 10.

V. CONCLUSION

We have presented a fully analytic theory for near-field thermal transfer via the nanoscale gap. A quantitative link between the heat transfer and the dispersion relations of the individual and the coupled surface waves has enabled us to have closed-form expressions of heat transfer coefficients. Our analysis has excellently captured the heat transfer behaviors for realistic materials such as SiC and graphene. Moreover, our results have revealed that 2D plasmons have a distinctive signature of $1/d$ dependency in near-field heat transfer at the nanoscale.

ACKNOWLEDGMENTS

Professor Fan's contribution to this publication was as a consultant and was not part of his Stanford duties or responsibilities.

[1] D. Polder and M. Van Hove, Phys. Rev. B **4**, 3303 (1971).
[2] K. Joulain, J.-P. Mulet, F. Marquier, R. Carminati, and J.-J. Greffet, Surf. Sci. Rep. **57**, 59 (2005).
[3] C. R. Otey, L. Zhu, S. Sandhu, and S. Fan, J. Quant. Spec. Rad. Trans. **132**, 3 (2014).
[4] D. G. Calhill, P. V. Braun, G. Chen, D. R. Clarke, S. Fan, K. E. Goodson, P. Keblinski, W. P. King, G. D. Mahan, A. Majumdar, H. J. Maris, S. R. Phillspot, E. Pop, and L. Shi, Appl. Phys. Rev. **1**, 011305 (2014).
[5] S.-A. Biehs, P. Ben-Abdallah, F. S. S. Rosa, K. Joulain, and J.-J. Greffet, Opt. Express **19**, A1088 (2011).
[6] M. Francoeur, S. Basu, and S. J. Petersen, Opt. Express **19**, 18774 (2011).
[7] S.-A. Biehs, M. Tschikin, and P. Ben-Abdallah, Phys. Rev. Lett. **109**, 104301 (2012).
[8] O. Ilic, M. Jablan, J. D. Joannopoulos, I. Celanovic, H. Buljan, and M. Soljacic, Phys. Rev. B **85**, 155422 (2012).
[9] V. B. Svetovoy, P. J. van Zwol, and J. Chevrier, Phys. Rev. B **85**, 155418 (2012).
[10] X. Liu, R. Z. Zhang, and Z. M. Zhang, ACS Photonics **1**, 785 (2014).
[11] A. Narayanaswamy and G. Chen, Phys. Rev. B **77**, 075125 (2008).
[12] C. Otey and S. Fan, Phys. Rev. B **84**, 245431 (2011).
[13] M. Kruger, T. Emig, and M. Kardar, Phys. Rev. Lett. **106**, 210404 (2011).
[14] H. Chalabi, E. Hasman, and M. L. Brongersma, Opt. Express **22**, 30032 (2014).
[15] Y. Zheng and A. Ghanekar, J. Appl. Phys. **117**, 064314 (2015).
[16] C. R. Otey, W. T. Lau, and S. Fan, Phys. Rev. Lett. **104**, 154301 (2010).
[17] S. Basu and M. Francoeur, Appl. Phys. Lett. **98**, 113106 (2011).
[18] H. Iizuka and S. Fan, J. Appl. Phys. **112**, 024304 (2012).
[19] R. Messina, M. Antezza, and P. Ben-Abdallah, Phys. Rev. Lett. **109**, 244302 (2012).

[20] P. Ben-Abdallah and S.-A. Biehs, Phys. Rev. Lett. **112**, 044301 (2014).
[21] V. Kubytskyi, S.-A. Biehs, and P. Ben-Abdallah, Phys. Rev. Lett. **113**, 074301 (2014).
[22] I. Latella, A. Perez-Madrid, J. M. Rubi, S.-A. Biehs, and P. Ben-Abdallah, Phys. Rev. Appl. **4**, 011001 (2015).
[23] H. Iizuka and S. Fan, J. Quant. Spec. Rad. Trans. **148**, 156 (2014).
[24] E. Rousseau, A. Siria, G. Jourdan, S. Volz, F. Comin, J. Chevrier, and J.-J. Greffet, Nature Photon. **3**, 514 (2009).
[25] S. Shen, A. Narayanaswamy, and G. Chen, Nano Lett. **9**, 2909 (2009).
[26] S. Shen, A. Mavrokefalos, P. Sambegoro, and G. Chen, Appl. Phys. Lett. **100**, 233114 (2012).
[27] Lu Hu, A. Narayanaswamy, X. Chen, and G. Chen, Appl. Phys. Lett. **92**, 133106 (2008).
[28] R. S. Ottens, V. Quetschke, S. Wise, A. A. Alemi, R. Lundock, G. Mueller, D. H. Reitze, D. B. Tanner, and B. F. Whiting, Phys. Rev. Lett. **107**, 014301 (2011).
[29] R. St-Gelais, B. Guha, L. Zhu, S. Fan, and M. Lipson, Nano Lett. **14**, 6971 (2014).
[30] K. Ito, A. Miura, H. Iizuka, and H. Toshiyoshi, Appl. Phys. Lett. **106**, 083504 (2015).
[31] J. Shi, B. Liu, P. Li, L. Y. Ng, and S. Shen, Nano Lett. **15**, 1217 (2015).
[32] M. Laroche, R. Carminati, and J.-J. Greffet, J. Appl. Phys. **100**, 063704 (2006).
[33] S. Basu, Z. M. Zhang, and C. J. Fu, Int. J. Energy Res. **33**, 1203 (2009).
[34] B. Guha, C. Otey, C. B. Poitras, S. Fan, and M. Lipson, Nano Lett. **12**, 4546 (2012).
[35] A. Kittel, W. Muller-Hirsch, J. Parisi, S.-A. Biehs, D. Reddig, and M. Holthaus, Phys. Rev. Lett. **95**, 224301 (2005).
[36] Y. De Wilde, F. Formanek, R. Carminati, B. Gralak, P.-A. Lemoine, K. Joulain, J.-P. Mulet, Y. Chen, and J.-J. Greffet, Nature **444**, 740 (2006).
[37] A. C. Jones and M. B. Raschke, Nano Lett. **12**, 1475 (2012).
[38] J. B. Pendry, J. Phys.: Condens. Matter **11**, 6621 (1999).
[39] S.-A. Biehs, E. Rousseau, and J.-J. Greffet, Phys. Rev. Lett. **105**, 234301 (2010).
[40] A. I. Volokitin and B. N. J. Persson, Phys. Rev. B **69**, 045417 (2004).
[41] S. Basu and Z. M. Zhang, J. Appl. Phys. **105**, 093535 (2009).
[42] P. Ben-Abdallah and K. Joulain, Phys. Rev. B **82**, 121419(R) (2010).
[43] O. D. Miller, S. G. Johnson, and A. W. Rodriguez, arXiv:1504.01323 (2015).
[44] L. A. Falkovsky, J. Phys. Conf. Ser. **129**, 012004 (2008).
[45] A. Perez-Madrid, J. M. Rubi, and L. C. Lapas, Phys. Rev. B **77**, 155417 (2008).
[46] S. Xiong, K. Yang, Y. A. Kosevich, Y. Chalopin, R. D'Agosta, P. Cortona, and S. Volz, Phys. Rev. Lett. **112**, 114301 (2014).
[47] A. Perez-Madrid, L. C. Lapas, and J. M. Rubi, PLoS ONE **8**, e58770 (2013).
[48] A. Archambault, M. Besbes, and J.-J. Greffet, Phys. Rev. Lett. **109**, 097405 (2012).
[49] J. B. Pendry, Phys. Rev. Lett. **85**, 3966 (2000).
[50] A. Raman, W. Shin, and S. Fan, Phys. Rev. Lett. **110**, 183901 (2013).
[51] M. Jablan, H. Buljan, and M. Soljacic, Phys. Rev. B **80**, 245435 (2009).
[52] F. H. L. Koppens, D. E. Chang, and F. J. Garcia de Abajo, Nano Lett. **11**, 3370 (2011).